International Journal of Fracture **58:** 93–114, 1992.

Brittle fracture of adhesive joints

A.R. AKISANYA and N.A. FLECK
Cambridge University Engineering Department,
Trumpington St., Cambridge, CB2 1PZ, England.

Received 1 August 1991; accepted 8 March 1992

Abstract. The effect of mode mix upon crack path is examined for a brittle epoxy adhesive. The mode mix is varied over wide limits by using asymmetrical double cantilever beam and Brazil nut specimen configurations. The observed crack paths are interfacial, in-layer, and alternating from one interface to the other in a periodic fashion. The probability of occurrence and toughness of each crack path is measured, and is compared with existing theory. Interfacial fracture is the most common path for all values of mode mix; the interfacial toughness increases dramatically with increasing mode II component of remote load. Under remote mode I loading the alternating crack path covers approximately 20 percent of the fracture surface of the specimens and has the highest macroscopic toughness. The effect of residual stress magnitude, layer thickness and mode mix upon the wavelength of the alternating crack mode is measured. Predictions based on a previous analysis by Akisanya and Fleck [1] compare favourably with the measured values.

1. Introduction

Electronic, automobile and aerospace components contain adhesive joints. A standard joint design is of sandwich type where two parts made from the same material are bonded by a thin adhesive layer. The reliability of the joint under mechanical and thermal stresses during processing and service constitute a major technical problem. Joints contain flaws. The observed strength of a joint depends upon the location and size of the flaws, and upon the crack path through the joint [2, 3, 4]. Typical crack paths are within the adhesive or substrate, or along the interface between the adhesive and a substrate. In this paper we investigate experimentally the toughness of an adhesive joint as a function of crack path.

Consider a sandwich type adhesive joint, containing an interfacial crack which is much longer than the adhesive thickness h, as shown in Fig. 1a. We assume that both substrates are made

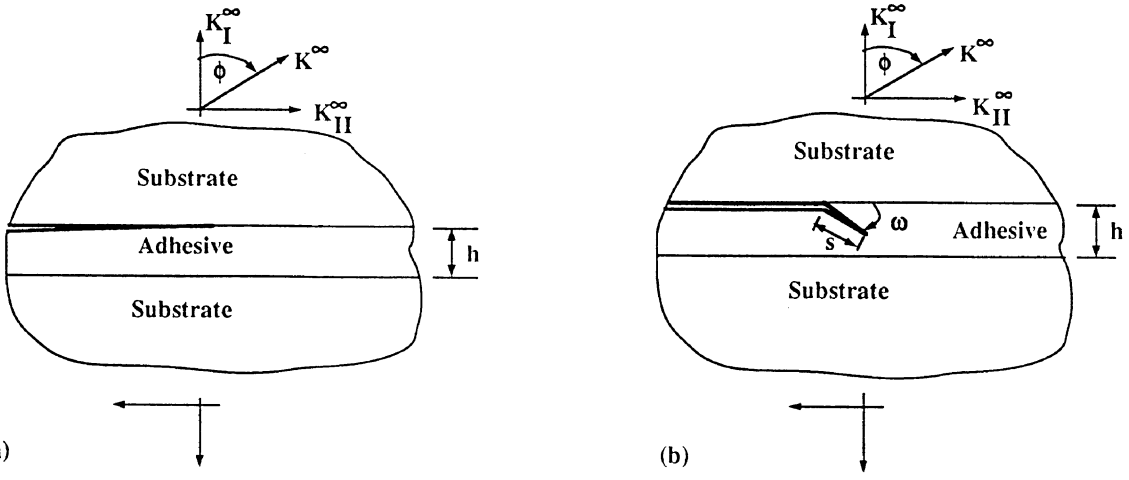

Fig. 1. (a) Interfacial crack between adhesive layer and substrate. (b) Interfacial crack with a kink in an adhesive joint.

from the same material, and behave in a linear elastic manner remote from the crack tip. At the macroscopic level, the toughness of the joint may be characterised by the remote stress intensity factors K_I^∞ and K_{II}^∞; these stress intensity factors are determined from the applied loads and geometry, neglecting the presence of the adhesive layer. The calibration for a large number of geometries has been cataloged for example by Tada et al. [5]. The remote stress intensity factors are the appropriate choice provided the crack length is much larger than all other length scales, including that of any inelastic zone in the adhesive or substrates surrounding the crack tip. The measured macroscopic toughness of an adhesive joint is dependent upon a number of variables including the crack path, the size of the crack tip plastic zone in comparison to the thickness of the adhesive layer, and the mode mix ϕ where,

$$\phi = \tan^{-1}(K_{II}^\infty / K_I^\infty). \tag{1}$$

The main observed crack paths for brittle adhesive joints are shown in Fig. 2. They are:

(a) interfacial between the adhesive and one of the substrates [6, 7],

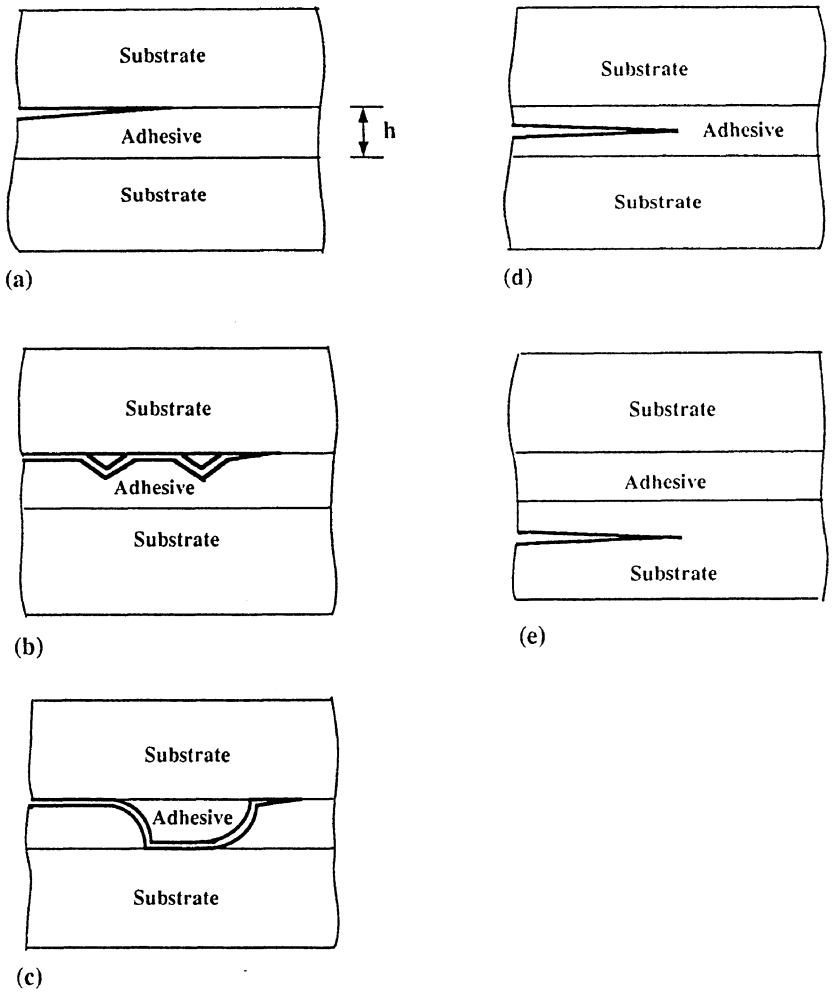

Fig. 2. Schematic diagrams of the possible failure paths in a sandwich specimen. (a) Interfacial failure, (b) Serrated interfacial failure, (c) Alternating crack, (d) In-layer failure parallel to the interface, and (e) Substrate failure parallel to the interface.

(b) in-layer, where the crack runs within the adhesive layer and parallel to the interface. The path adopted may be near to the centre line of the adhesive layer [8], or adjacent to one of the interfaces [9, 10],
(c) in one of the substrates and parallel to the layer [10], and
(d) alternating from one interface to the other through the adhesive layer [1, 11].

The purpose of the present paper is to investigate the effect of the mode mix ϕ upon the relative frequency of occurrence of the above crack paths for a brittle epoxy layer (Ciba Geigy type F922), sandwiched between aluminium alloy substrates. The F922 epoxy is elastic-brittle and is used as a base ingredient in a number of epoxy matrices for composite materials. We are thus able to exclude the effects of crack tip plasticity upon crack path selection and the observed toughness. The aluminium-epoxy system is a useful model material for investigating the role of crack path on the toughness of ceramic-ceramic joints.

The structure of the paper is as follows. First, some essentials of interfacial fracture mechanics are reviewed. We report toughness tests on the aluminium-epoxy system, using asymmetrical double cantilever beam (DCB) and Brazil nut sandwich specimens. The mode mix is controlled by the relative height of each arm of the DCB specimens, and by the orientation of the Brazil nut specimens. The cracking paths are reported, and observations of crack path as a function of mode mix are compared with theoretical predictions from the literature. Particular attention is paid to the effect of adhesive layer thickness, residual stress magnitude and mode mix upon the wavelength and toughness of the alternating crack path.

2. Interfacial fracture mechanics

We shall require some basic results for interfacial cracks in order to interpret the results for cracks along the interface between the adhesive layer and one of the substrates. Consider an interfacial crack between two isotropic elastic solids 1 and 2. Later we shall identify materials 1 and 2 with the substrate and adhesive layer, respectively. The elastic mismatch between the two materials is governed by the following parameters under plane stain conditions [12]

$$\alpha = \frac{(1-\nu_2)/\mu_2 - (1-\nu_1)/\mu_1}{(1-\nu_2)/\mu_2 + (1-\nu_1)/\mu_1},$$

$$\beta = \frac{1}{2}\frac{(1-2\nu_2)/\mu_2 - (1-2\nu_1)/\mu_1}{(1-\nu_2)/\mu_2 + (1-\nu_1)/\mu_1}, \tag{2}$$

$$\varepsilon = \frac{1}{2\pi}\ln\left(\frac{1-\beta}{1+\beta}\right),$$

where μ is the shear modulus, ν is Poisson's ratio, and the subscripts 1 and 2 refer to the materials 1 and 2, respectively.

An oscillatory singularity exists at the crack tip, such that the relative proportion of shear stress to normal stress varies with distance from the crack tip. In order to define the mode mix, we consider the ratio of shear stress to normal stress at a fixed distance $\hat{l}$ from the crack tip, as

suggested by Rice [13]. The mode mix $\hat{\psi}$ for the interfacial crack is defined by

$$\hat{\psi} = \arctan\left(\frac{\mathrm{Im}(\mathbf{K}\hat{l}^{i\varepsilon}}{\mathrm{Re}(\mathbf{K}\hat{l}^{i\varepsilon})}\right), \tag{3}$$

where **K** is the (complex) interfacial stress intensity factor. It does not matter how the fixed length $\hat{l}$ is chosen provided the chosen value is reported along with the experimental interfacial toughness results. If two different fixed length values $\hat{l}_1$ and $\hat{l}_2$ are used in reporting the same interfacial toughness results, there would be a translation $\hat{\psi}_2 - \hat{\psi}_1 = \varepsilon \ln(\hat{l}_2/\hat{l}_1)$ in the $\hat{\psi}$ co-ordinate. In the present study, we choose arbitrarily a value $\hat{l} = 100\ \mu\mathrm{m}$.

The mode mix $\hat{\psi}$ for the interfacial crack in the sandwich specimen may be related to the mode mix ϕ for the homogeneous base specimen [14]. For the case of an interfacial crack laying in the upper interface of the sandwich specimen, Suo and Hutchinson [14] showed that

$$\hat{\psi} = \phi + \varepsilon \ln\left(\frac{\hat{l}}{h}\right) + \Omega, \tag{4}$$

where Ω depends only upon α and β, and has been cataloged by Suo and Hutchinson [14]. For the aluminium/epoxy sandwich specimens used here, $\alpha = 0.89$, $\beta = 0.17$, and $\Omega = -13^\circ$ when the crack is on the upper interface.

2.1. Kinking from an interface

Consider an adhesive joint under remote loading K_{I}^{∞} and K_{II}^{∞}. An interfacial crack exists at the upper interface and is subjected to a loading phase angle $\hat{\psi}$. A kink-like flaw of length s and orientation ω exists at the tip of the interfacial crack, see Fig. 1b. A sufficient condition for the interfacial crack to kink out of the interface of toughness $\Gamma_I(\hat{\psi})$ into an adjacent material of toughness Γ_s is given by [15],

$$\frac{\Gamma_I(\hat{\psi})}{\Gamma_S} \geqslant \frac{G_I}{G_s^*} \tag{5}$$

where G_I is the energy release rate along the interface and G_s^* is the energy release rate at the tip of a kink orientated such that $K_{\mathrm{II}} = 0$ at its tip. In order for the kink to grow away from the interface and across the layer, the stress intensity factors at the kink tip must satisfy the condition $K_{\mathrm{I}} > 0$, $K_{\mathrm{II}} \geqslant 0$. A kink with $K_{\mathrm{II}} < 0$ is driven back toward the interface.

3. Test method

Asymmetrical double cantilever beam and Brazil nut sandwich specimens were manufactured from 2014A-T aluminium alloy substrates and Ciba Geigy 922 adhesive. The uniaxial tensile response of the bulk adhesive at a strain rate of $1.6 \times 10^{-5}\ \mathrm{s}^{-1}$ is shown in Fig. 3. It is almost linear elastic up to a failure strain of 1.2 percent, with a Young's modulus $E = 3.8\ \mathrm{GPa}$ and

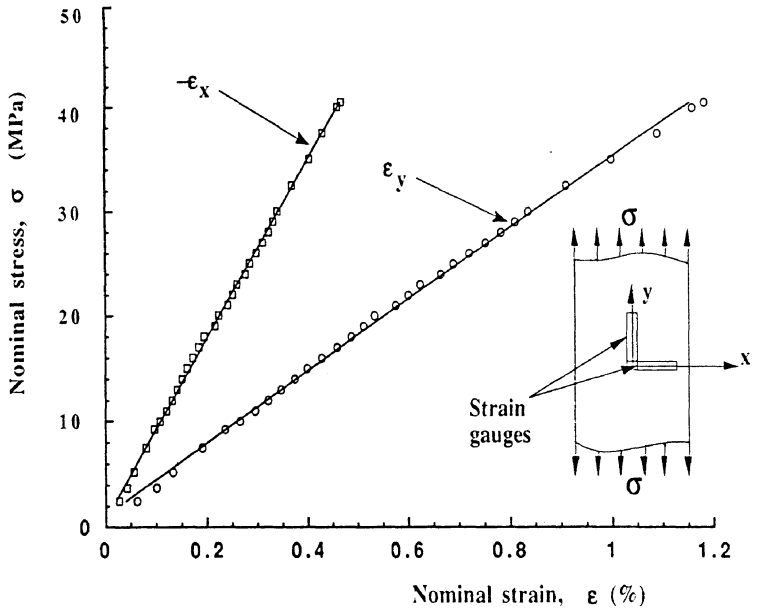

Fig. 3. Nominal stress versus nominal strain for Epoxy 922. The test was conducted at a strain rate of $1.6 \times 10^{-5}\,s^{-1}$. The solid lines show a linear fit to the data.

Poisson's ratio $\nu = 0.38$. The plane strain mode I toughness of the epoxy was measured using 4 mm thick four-point bend specimens. The specimens were manufactured by successively laying down 1 mm thick layers of epoxy at a cure temperature of 160°C. We found that the toughness of the epoxy is $\Gamma_s = 43 \pm 8\,Jm^{-2}$.

The aluminium alloy has the following properties: $E = 70$ GPa, $\nu = 0.35$ and 0.1 percent offset yield stress $\sigma_y = 100$ MPa. The coefficient of thermal expansion of the epoxy and aluminium was determined by heating the materials in an oven and measuring the thermal strain. We found that the coefficient of thermal expansion ρ is $5.8 \times 10^{-5}\,K^{-1}$ for the epoxy, and $\rho = 2.1 \times 10^{-5}\,K^{-1}$ for the aluminium alloy.

3.1. Asymmetrical double cantilever beam specimens

The DCB geometry is shown in Fig. 4a. We machined strips of aluminium alloy of length 200 mm and thickness $t = 10$ mm. For the symmetrical DCB specimens, the two arms are of the same height $h_1 = h_2 = 6.5$ mm, the geometry is symmetric about the centre line of the adhesive layer and the phase angle $\phi = 0°$ by symmetry. For the asymmetric specimens the height of the arms h_1 and h_2 was varied from 6.5 mm to 26 mm. In this way we were able to vary ϕ so that it lay in the range $-24°$ to 24°. The calibration for the remote stress intensity factors has been given recently by Bao et al. [16] and is summarised in Appendix A.

A starter crack of length L exists along the upper interface of the joint, and a load P per unit thickness is applied to the top and bottom arms. The specimens were pin loaded, and were tested at a constant crosshead speed of $0.01\,mm\,s^{-1}$. The crack length was measured using a travelling microscope, and the crack length, crosshead displacement and applied load were recorded.

3.2. Brazil nut specimens

Brazil nut specimens were manufactured from semi-circular aluminium alloy disks of radius $R = 30$ mm, and thickness $t = 6.5$ mm. A starter crack of length $2L$ was made along the upper

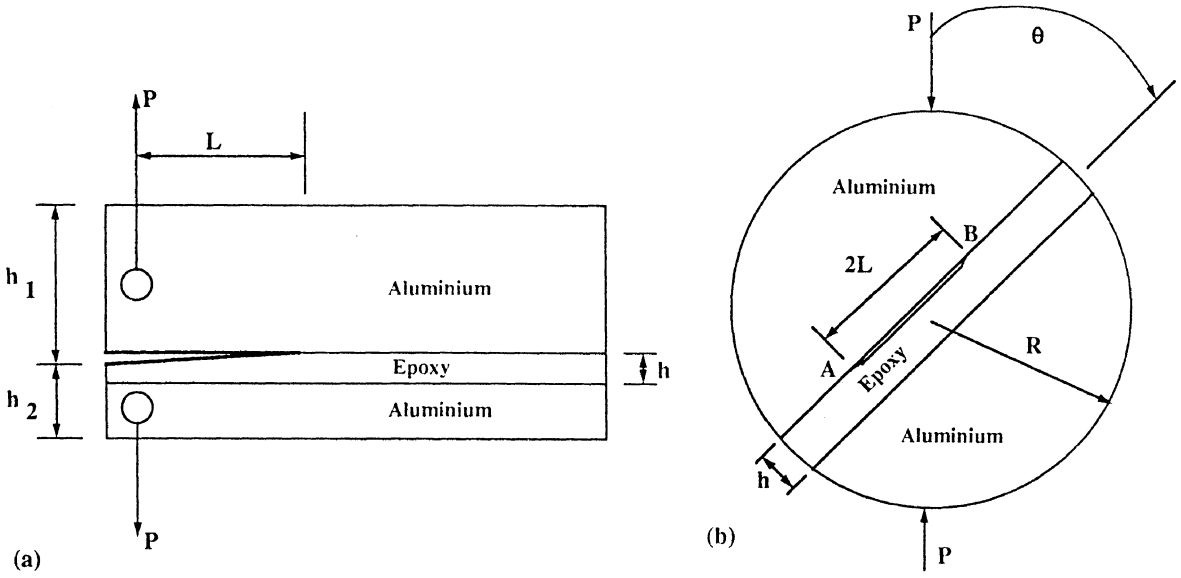

Fig. 4. Specimen geometries (a) Asymmetric DCB specimen, and (b) Brazil nut specimen.

interface of the adhesive layer, as shown in Fig. 4b. The mode mix ϕ was controlled by the compression angle θ. The specimen is in mode I ($\phi = 0°$) when $\theta = 0°$, and is in pure mode II ($\phi = 90°$) when $\theta \sim 25°$. We varied the diametral angle θ from 5° to 20°, giving $\phi = 23°$ to $\phi = 77°$. A detailed analysis of the homogeneous specimen is given by Atkinson et al. [17] for the isotropic case, and by Liaw and Kamel [18] for anisotropic disks. The specimen calibration is given in Appendix A. The loading points were lubricated in order to minimise the effects of friction. Compression tests were conducted at a crosshead speed of 0.001 mm s^{-1}.

3.3. Application of adhesive

For both the DCB and Brazil nut geometries, the bonding surfaces of the aluminium alloy were polished using a 1000 grit silicon carbide emery paper. The surfaces were degreased with acetone, and chemically etched in sulphuric acid-sodium dichromate solution prior to bonding. An initial crack was introduced into the joint by contaminating one of the bonding surfaces with graphite powder and a silicone release agent. This was done over a length $L = 30$ mm at one end of the DCB specimens, and over a length $2L = 24$ mm at the centre of the Brazil nut specimens. The epoxy adhesive was then heated to its flow temperature of 75°C and applied to the bonding surfaces. The two halves of the specimen were clamped together in order to exclude air bubbles, and the bond thickness h was controlled by spacers placed at each end of the joint. In general the specimens were cured at a temperature of 160°C for 3 hours and air-cooled to room temperature. After cure, the adhesive layer thickness was measured at 5 points along the specimen length using a travelling microscope. Specimens with a thickness variation of more than 10 percent along their length were rejected.

We investigated the effects of the thickness of the adhesive layer and the level of residual tensile stress in the layer upon the crack path and macroscopic toughness, using the symmetric DCB specimens ($\phi = 0°$). Three layer thicknesses were used ($h = 0.2$ mm, 0.4 mm, and 0.6 mm), and four different values of residual tensile stress were induced by varying the cure cycle. For the DCB specimens the mean thickness of the adhesive layer was within 5 percent of the desired value. The cure cycles are summarised in Table 1. The residual stress σ_0 in the adhesive layer

Table 1: Cure cycles

Case	Cure cycle	Estimate of σ_0 (MPa)
A	Cured at 120°C for 6 hours and air-cooled to room temperature in 20 minutes.	22.7
B	Dwelled at 120°C for 1 hour. Cured at 160°C for 3 hours and air-cooled to room temperature in 30 minutes.	31.8
C	Dwelled at 120°C for 1 hour. Cured at 190°C for 2 hours and air-cooled to room temperature in 35 minutes.	38.6
D	Dwelled at 120°C for 1 hour. Cured at 150°C for 3 hours. Cooled slowly to room temperature in the oven over a period of 20 hours. Left for 24 hours. Recured at 220°C for 2 hours and air-cooled to room temperature in 45 minutes.	45.4

with coefficient of thermal expansion ρ_2, Young's modulus E_2 and Poisson's ratio v_2 is estimated to be

$$\sigma_0 = \frac{E_2}{1 - v_2}(\rho_2 - \rho_1)\Delta T, \tag{6}$$

where ρ_1 is the coefficient of thermal expansion of the aluminium alloy substrate and ΔT is the difference between the cure temperature and room temperature. Estimated values for σ_0 are included in Table 1.

The effect of loading phase ϕ upon crack path and macroscopic toughness was determined for the asymmetric DCB specimens using $h = 0.4$ mm, and for the Brazil nut specimens using $h = 0.09$–0.4 mm. Control of the layer thickness was imprecise for the Brazil nut specimens due to difficulties in clamping the two substrates together during cure of the adhesive. However, the layer thickness was measured accurately after cure, as described above.

4. Results

4.1. Selection of crack path: DCB specimens

In general, crack growth in the symmetric and asymmetric DCB specimens was stable using a screw driven test machine in displacement control. Approximately 20 values of load and crack length were measured for each specimen. Four characteristic load versus deflection responses were observed, Fig. 5, corresponding to the four main cracking paths:

1. Interfacial failure,
2. Serrated interfacial failure
3. In-layer failure, and
4. Alternating crack pattern where the crack kinks periodically from one interface to the other.

Typical examples of the fracture surfaces associated with each of the cracking patterns are shown in Fig. 6. Discrete load drops are an intrinsic feature of the serrated and alternating crack paths, and correspond to kinking of the interfacial crack into the adhesive layer. Small bursts of unstable crack growth occasionally accompanied interfacial and in-layer crack growth; these occur when the crack tip encounters a zone of relatively low toughness. In cases where crack

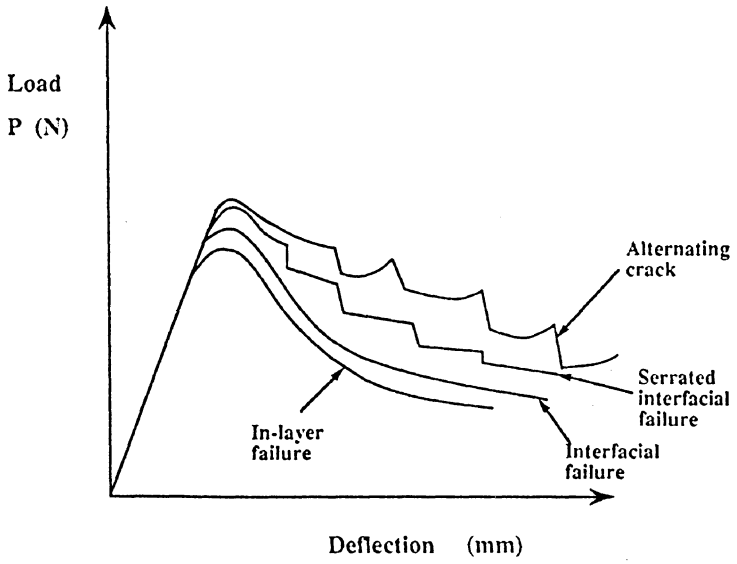

Fig. 5. Schematic diagram of the load-displacement curve for the DCB specimen showing the effect of local cracking pattern.

jumps occurred, the load and crack length immediately prior to the load drop were used to calculate the toughness. The increased load associated with the interfacial and alternating crack morphologies compared with in-layer fracture is associated with higher toughness paths.

We frequently observed that the cracking pattern changed over a distance of the order of $100h$ in the same DCB specimen. The relative proportion of fracture surface created by the various crack paths for the DCB specimens is shown as a function of phase angle ϕ in Fig. 7, for the case $\sigma_0 = 31.8$ MPa, and $h = 0.4$ mm. The interfacial mode of growth is the most frequently

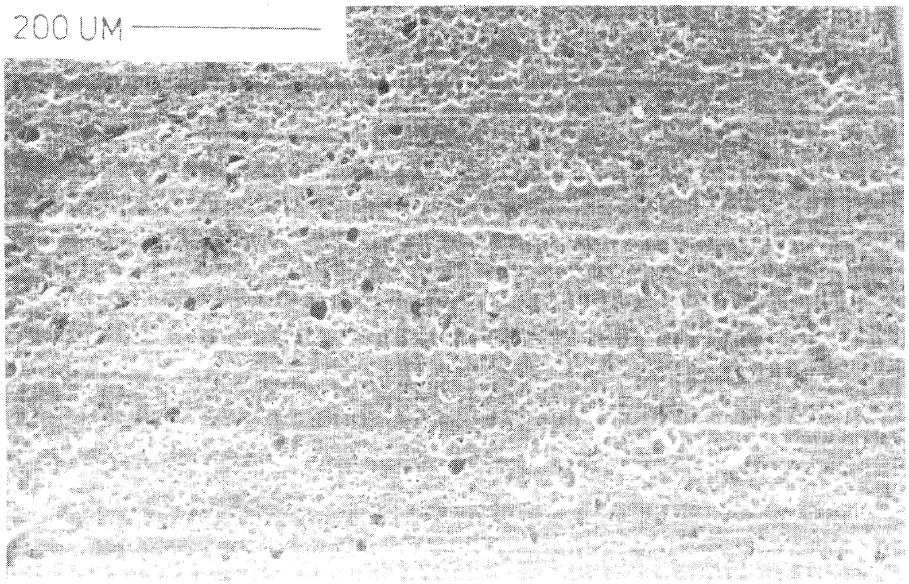

Fig. 6a.

Fig. 6. Fracture surfaces of all the failure modes of the DCB specimens. (a) Interfacial failure showing the adherend side, (b) Serrated interfacial failure ($\sigma_0 = 31.8$ MPa, $h = 0.4$ mm), (c) In-layer failure parallel to the interface and near the center of the joint, (d) In-layer failure near and parallel to the interface, (e) Alternating crack ($\sigma_0 = 38.6$ MPa, $h = 0.4$ mm), and (f) Magnified view of the circled part of Fig. 6e showing the crack curvature as it approaches the interface. The arrow on Fig. 6e indicates the point where the crack leaves the interface. The crack propagation is from the left to the right in all cases.

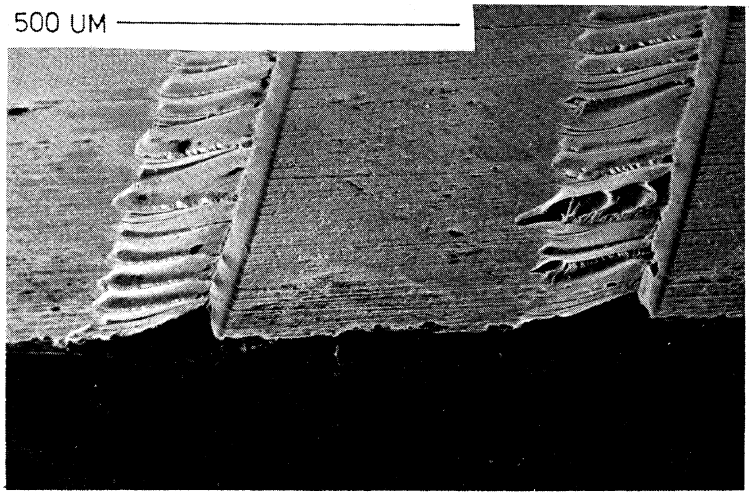

Fig. 6b.

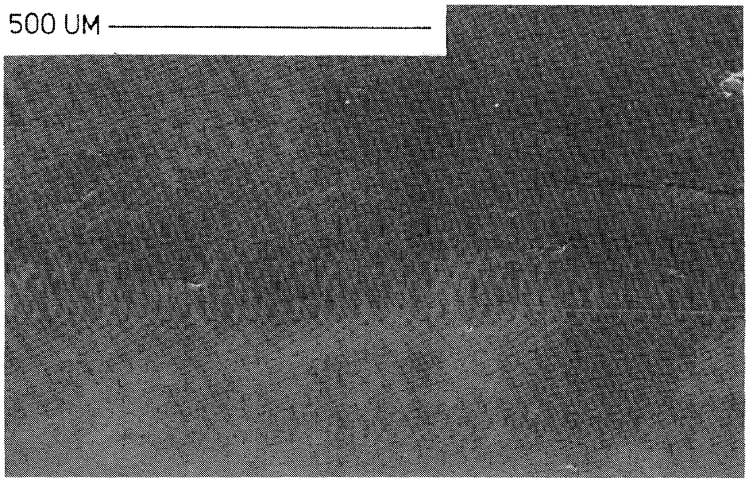

Fig. 6c.

Fig. 6d.

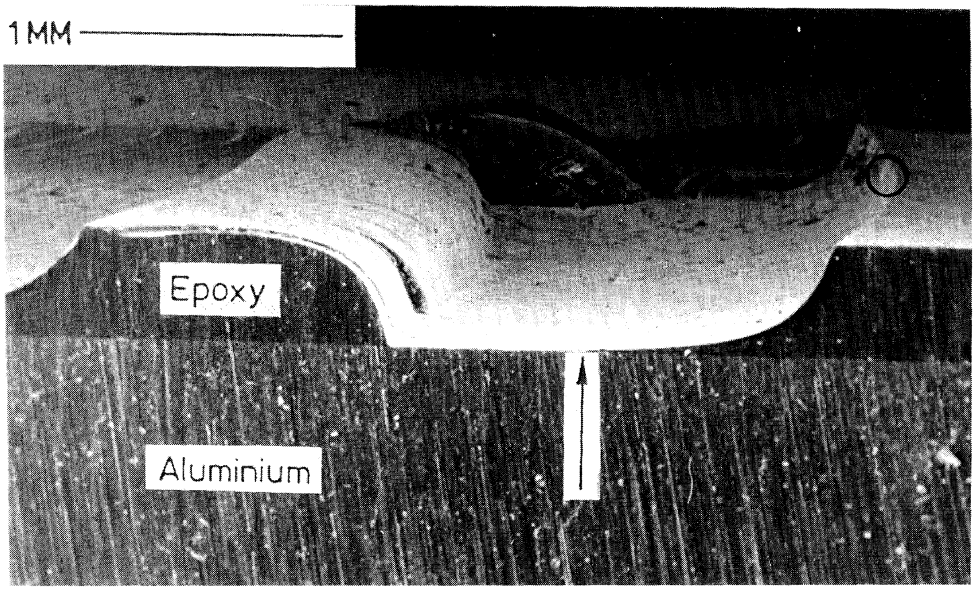

Fig. 6e.

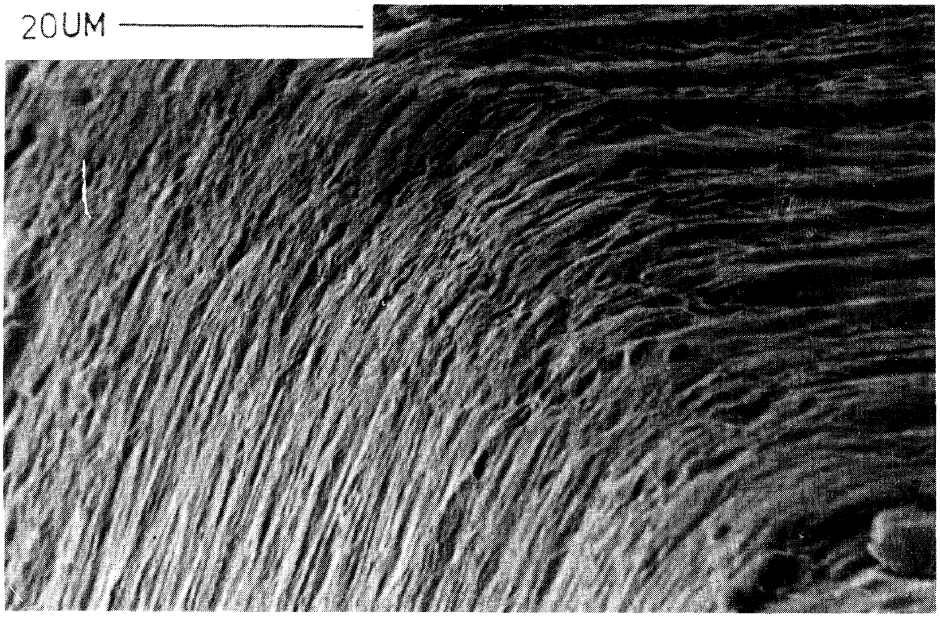

Fig. 6f.

encountered at small phase angles, and becomes the only mode observed at large absolute values of ϕ.

4.2. Selection of crack path: Brazil nut specimens

The Brazil nut specimens deformed linearly with respect to applied load, until crack initiation and catastrophic fracture intervened; in all cases, the crack grew dynamically. Four specimens were tested at each diametral angle. Three failure patterns were distinguished as shown in Fig. 8. We shall show later that the interfacial toughness curve $\Gamma_I(\hat{\psi})$ is approximately symmetric about $\hat{\psi} = 7.5°$; this leads us to conclude that crack propagation starts at tip A rather than tip B for the three failure patterns. Type I failure occurs when $\hat{\psi}$ is large ($\hat{\psi} > 50°$) for crack tip A; the

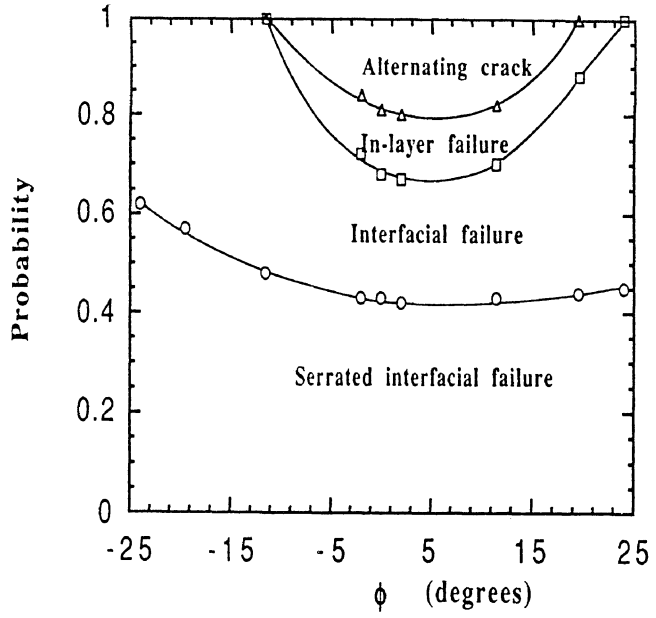

Fig. 7. Effect of remote phase angle $\phi = \arctan(K_{II}^{\infty}/K_{I}^{\infty})$ on the probability of occurrence of the various failure patterns in the DCB specimens. $\sigma_0 = 31.8$ MPa, $h = 0.4$ mm.

crack tip A kinks across the adhesive layer, while crack tip B suffers a large negative phase angle ($\hat{\psi}_B < 0$) and propagates as an interfacial crack. We do not present interfacial toughness data corresponding to this failure mode as the critical event is the initiation of kinking from crack tip A. A similar dependence of crack extension path on the sign of the loading phase angle has been observed by Cao and Evans [6].

For intermediate phase angles, $20° \leqslant \hat{\psi} \leqslant 50°$, crack tip A ran along the upper interface for a small distance and then kinked into the lower interface. Crack tip B propagated as an interfacial crack under negative $\hat{\psi}$. We term this a type II failure.

In the third failure mode, type III, crack tips A and B propagated interfacially. In this regime, the phase angle for crack tip A was small, $0° < \hat{\psi} < 20°$. This failure mode is the preferred one when measuring interfacial toughness.

4.3. Interfacial fracture

The DCB and Brazil nut specimens used for the determination of the interfacial toughness were cured at 160°C for 3 hours, and air cooled to room temperature; this corresponds to case B of Table 1 and results in a residual tensile stress level of $\sigma_0 = 31.8$ MPa in the adhesive layer. The measured interfacial toughness response $\Gamma_I(\hat{\psi})$ is shown in Fig. 9. We observed no effect of the adhesive layer thickness upon the observed interfacial toughness.

The residual stress level in symmetric DCB specimens ($\phi = 0°$, $\hat{\psi} = -10°$) was varied from $\sigma_0 = 22.7$ MPa to $\sigma_0 = 45.4$ MPa via the four different cures summarised in Table 1. No effect of residual stress upon the interfacial toughness was noted.

We observed that the interfacial toughness increases as the proportion of shear loading increases, see Fig. 9, in agreement with previous observations, for example [6, 7, 8, 19]. The higher toughness at larger absolute values of $\hat{\psi}$ has been attributed to various factors including crack face friction at asperities [20] and crack face contact due to the effect of the oscillatory index ε.

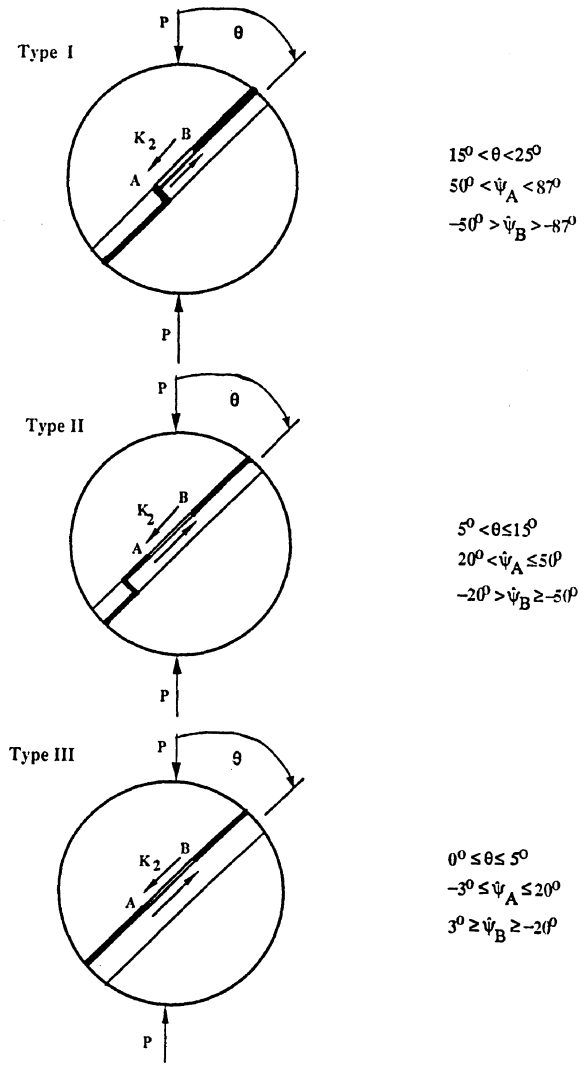

Fig. 8. Schematic diagrams of the failure patterns for the Brazil nut specimens. The direction of the 'mode 2' interfacial stress intensity factor K_2 is included. K_2 is positive at crack tip A and negative at tip B.

An empirical curve fit which fits the interfacial toughness curve $\Gamma_I(\hat{\psi})$ has been suggested by Hutchinson and Suo [21]. It takes the form,

$$\Gamma_1(\hat{\psi}) = \Gamma_1^c[1 + (1 - n)\tan^2 \hat{\psi}], \tag{7}$$

where Γ_1^c is the 'mode I' toughness of the interface, and the parameter n measures the influence of shear deformations on the observed toughness. The limit $n = 1$ corresponds to an ideally brittle interface where $\Gamma_I(\hat{\psi}) = \Gamma_1^c$ for all values of $\hat{\psi}$. When $n = 0$, crack growth depends only on the 'mode I' component of the crack tip loading.

The predictions of (7) for $n = 0$ and $n = 0.5$ are compared with the measured $\Gamma_I(\hat{\psi})$ response in Fig. 9. We choose Γ_1^c to coincide with $\Gamma_1(\hat{\psi} = 0)$. The curve fit with $n = 0$ approximately fits the data for $\hat{\psi} > 0$, but fails for $\hat{\psi} < 0$. We note that the empirical fit to $\Gamma_I(\hat{\psi})$ is symmetric about $\hat{\psi} = 0$, whereas the measured $\Gamma_I(\hat{\psi})$ response is unsymmetric about $\hat{\psi} = 0$. In general we do not expect the interfacial toughness response to be symmetric about the $\hat{\psi} = 0$ axis, since the value of the loading phase depends upon the chosen value of length scale $\hat{l}$ used in defining $\hat{\psi}$. Furthermore,

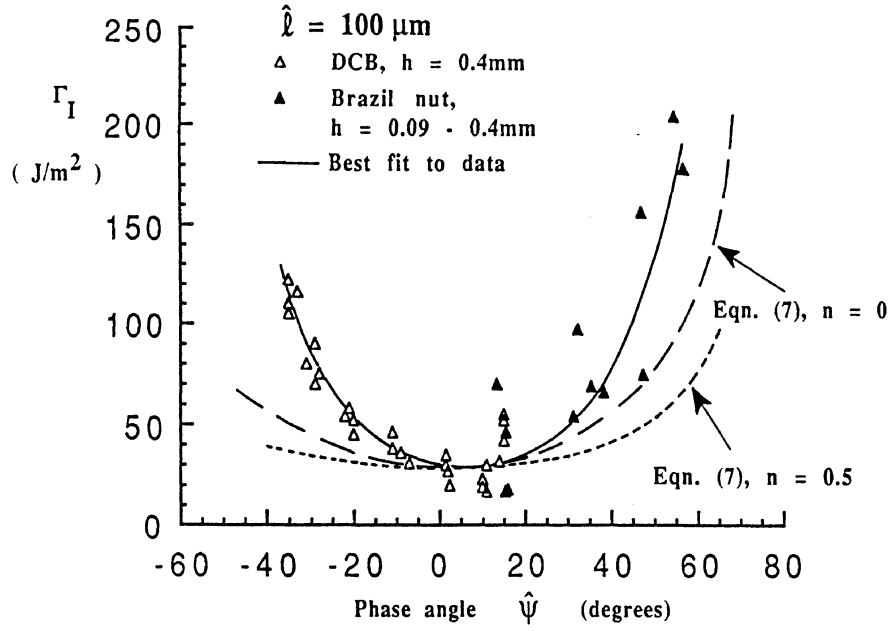

Fig. 9. Interfacial toughness curve. The data points correspond to the average values of the macroscopic toughness when the crack propagation is rectilinear and along the interface. The maximum standard deviation is 12 percent of the average value. $\sigma_0 = 31.8$ MPa.

the interface may possess a different toughness when an interfacial crack runs in two opposing directions, due for example to directionality of the interfacial roughness. In the present study, surface roughness profiles of the aluminium substrates were measured prior to bonding, using a Ferranti Surfcom. The centre-line-average roughness was 0.7 μm, and no directionality of the surface profile was detected from roughness traces.

The He and Hutchinson kinking analysis [15] suggests that an interfacial crack remains in the interface when the left hand side of (5) is less than the right hand side. For the $\Gamma_I(\hat{\psi})/\Gamma_s$ response shown in Fig. 9, the left hand side of (5) equals the right hand side at $\hat{\psi} = 19°$. This is in good agreement with the observed crack trajectories in the Brazil nut tests: the crack remains in the interface (type III crack pattern) when $\hat{\psi}_A \leqslant 20°$.

4.4. Serrated interfacial crack path

The interfacial crack occasionally interacted with pre-existing flaws at an angle $\omega = 10° - 15°$ to the interface. The flaws kinked back to the interface, and resulted in a serrated crack path as shown in Fig. 6b. When the flaws were numerous, the serrations occurred with a spacing of $3h$–$10h$, and we term the crack path a serrated interfacial path.

The mode II stress intensity factor K_{II} at the tip of the flaw in the adhesive layer is negative for most angles $\omega > 0°$ when the main interfacial crack is subjected to a loading $\hat{\psi} < 0$ [15]. Thus the flaw kinks back towards the interface and results in the serrated crack path. The macroscopic toughness of the serrated crack path was approximately 20 percent greater than that of the unserrated interfacial crack path as shown in Fig. 10. A possible explanation for this is the locking of the fracture surfaces at the serrations under remote mixed mode loading.

The stored elastic energy per unit area in the uncracked adhesive layer of thickness h, and under residual stress σ_0 is $(1 - \nu_2)\sigma_0^2 h/E_2$, while the energy required to form unit area of

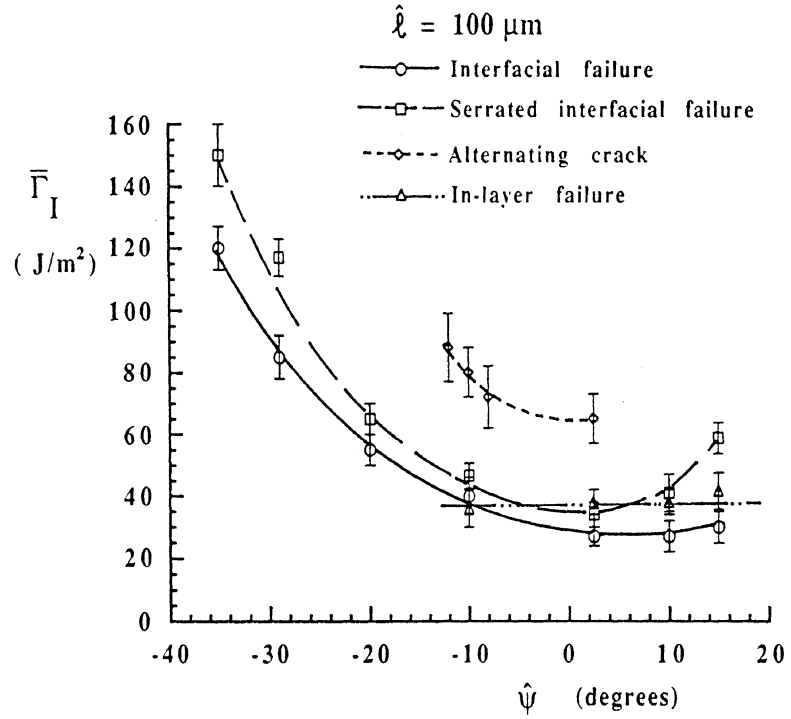

Fig. 10. Effect of loading and the crack path upon the average macroscopic toughness $\bar{\Gamma}_I$ of the DCB specimens. $\sigma_0 = 31.8$ MPa, $h = 0.4$ mm.

interfacial crack is $\Gamma_I(\hat{\psi})$. We introduce the non-dimensional parameter $\xi = \sigma_0\sqrt{h}/\sqrt{\bar{E}_2\Gamma_I(\hat{\psi})}$ as a measure of the stored elastic strain energy in the layer. The average macroscopic toughness increases slightly with inceasing residual stress level characterised by $\xi = \sigma_0\sqrt{h}/\sqrt{\bar{E}_2\Gamma_I(\hat{\psi})}$, see Fig. 11. The frequency of occurrence of the serrated crack path increases slightly with absolute magnitude of phase angle $\hat{\psi}$, see Fig. 7, and with increasing layer thickness h.

4.5. *In-layer fracture*

The crack occasionally grew within the adhesive layer and parallel to the interface. The relative frequency of occurrence of the in-layer path is summarised in Fig. 7. The presence of a large remote mode II stress intensity factor drove the in-layer crack to the interface and interfacial fracture superceded in-layer failure.

The measured toughness of the in-layer paths was in the range 25–45 Jm^{-2}, and was equal to the bulk toughness of the epoxy $\Gamma_s = 43 \pm 8\ \mathrm{Jm}^{-2}$ to within experimental scatter. This supports the conclusion that plasticity effects can be neglected for this highly brittle epoxy system. When $|K_{II}^{\infty}/K_I^{\infty}|$ was less than approximately 0.05, the in-layer crack grew along two possible paths: near to the centre line of the adhesive (Fig. 6c), and adjacent to the interface (Fig. 6d). When the mode mix was increased the in-layer crack propagated close to the lower interface.

Fleck et al. [10] have shown that a compliant adhesive joint loaded in remote mode I has three possible in-layer crack paths. It is assumed that the in-layer crack positions itself at a location of zero mode II stress intensity factor at the crack tip. Two of the locations are near the interface while the third is along the centre line of the adhesive layer, as shown in Fig. 12. When the remote mode mix is increased a single mode I path exists close to the lower interface. The

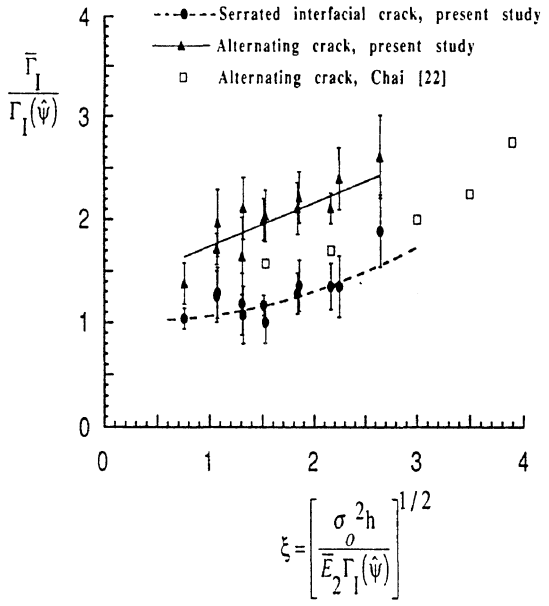

Fig. 11. Effect of crack path and the residual stress σ_0 upon the average macroscopic toughness $\bar{\Gamma}_I$ of the aluminium/epoxy joint under a remote mode I loading. $\Gamma_I(\hat{\psi})$ is the interfacial toughness when the crack propagation is rectilinear and along the interface.

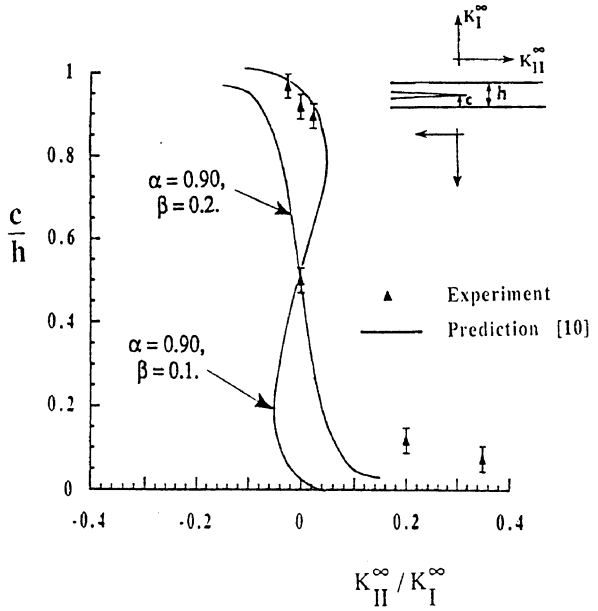

Fig. 12. The location of the in-layer crack satisfying $K_{II} = 0$ as a function of $K_{II}^\infty / K_I^\infty$ for the aluminium/epoxy joint. $\alpha = 0.89$, $\beta = 0.17$.

predicted paths are in good agreement with the observed paths, see Fig. 12. Fleck et al. [10] argue that the stability of any of the paths depends upon the sign of the non-singular stress parallel to the crack surface at the crack tip, normally referred to as the '*T*-stress'. The path is stable when the *T*-stress is negative and is unstable when the *T*-stress is positive. For the current tests, evaluation of the *T*-stress showed it to be positive for the range of σ_0 and h considered. Therefore, the crack is unable to run a large distance within the adhesive layer. This is consistent with observations: the in-layer cracks existed over lengths of a few mm.

There was no observed effect of layer thickness h, or residual stress level σ_0 on the observed toughness of the in-layer crack path.

4.6. Alternating crack path

Akisanya and Fleck [1] have analysed the alternating crack path by the finite element method. They show that the alternating crack path is due to periodic kinking of an interfacial crack whereby the crack departs from one interface and grows across the layer until it becomes an interfacial crack on the opposing interface. The crack kinks away from the interface when the interfacial phase angle at the crack tip attains a critical value, in accordance with the theory of He and Hutchinson [15]. The argument is summarised below.

The alternating crack trajectory is idealised by a semi-infinite crack in an infinite layered body in Fig. 13a. The idealised crack contains a single kink through the layer at $x = -l$, such that the crack lies along the lower interface from $x = -l$ to $x = -\infty$, and along the upper interface for $-l < x < 0$. The specimen is loaded remotely by a remote stress intensity factor $K^\infty = K_I^\infty + iK_{II}^\infty$ for the homogeneous base specimen neglecting the presence of the layer. Also, a residual tensile stress σ_0 exists in the adhesive layer of thickness h. The interfacial

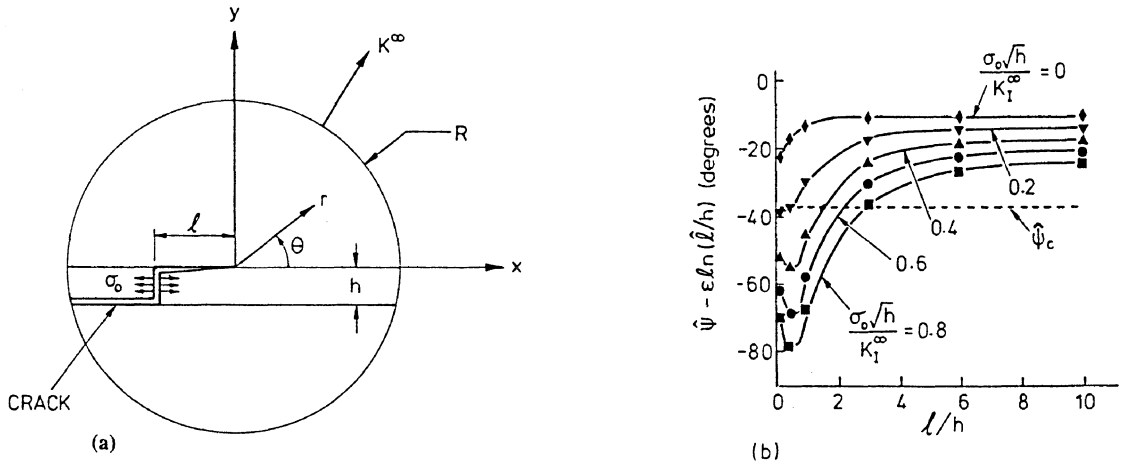

Fig. 13. The alternating crack. (a) Idealised geometry, and (b) The effect of relative crack length l/h and the non-dimensional residual stress $\sigma_0\sqrt{h}/K_I^\infty$ upon the interfacial phase angle $\hat{\psi} = \arctan\,[\mathrm{Im}(\mathbf{K}\hat{l}^{i\varepsilon})/\mathrm{Re}(\mathbf{K}\hat{l}^{i\varepsilon})]$. $\hat{\psi}_c$ is for $s/\hat{l} = 0.01$, $\alpha = 0.80$, and $\beta = 0.20$.

stress intensity factor **K** at the tip of the crack as it grows away from the previous kink is given by [1]

$$\mathbf{K}\hat{l}^{i\varepsilon} = (\hat{l}/h)^{i\varepsilon} aK^\infty + (\hat{l}/h)^{-i\varepsilon}\overline{bK^\infty} + (\hat{l}/h)^{i\varepsilon} e\sigma_0\sqrt{h}, \tag{8}$$

where a, b and e are non-dimensional complex functions of α, β, and l/h and are tabulated in [1].

Under fixed remote loading σ_0 and K^∞, the phase angle $\hat{\psi}$ of the interfacial crack, defined by (3), increases with growth of the interfacial crack. This is shown in Fig. 13b. In practice, the remote loading K^∞ on a specimen is not held constant, but is adjusted by load shedding of the specimen in order for the energy release rate G_I at the interfacial crack tip to equal the interfacial toughness $\Gamma_I(\hat{\psi})$; when this is taken into account, we still find that $\hat{\psi}$ increases with crack extension from the previous kink. The interfacial crack kinks out of the interface and into the adhesive layer when the phase angle $\hat{\psi}$ attains a critical value $\hat{\psi}_c$ which is deduced from the kinking theory of He and Hutchinson [15] as follows. Observations show that the alternating crack trajectory leaves the interface smoothly. This suggests that the dominant flaws of length s on the aluminium-epoxy interface exist at a vanishingly small angle $\omega = 0°$, as shown in Fig. 6e. A necessary condition for kinking of the main interfacial crack out of the interface is that the stress intensity factors at the kink tip suffer the condition $K_I > 0$, $K_{II} \geqslant 0$, since a kinked crack with $K_{II} < 0$ is driven back toward the interface. Examination of the He and Hutchinson [15] kinking analysis shows that this necessary condition is first satisfied when $\hat{\psi}$ attains a value $\hat{\psi}_c$, which corresponds to the case of $K_{II} = 0$ at the tip of a kink with an orientation $\omega = 0°$ to the interface. $\hat{\psi}_c$ is a function of the elastic parameters α and β, and $s/\hat{l}$. For aluminium/epoxy, $\hat{\psi}_c = -29°$ for the case $s/\hat{l} = 0.1$.

We conclude that the wavelength of the alternating crack trajectory l_c is controlled by the condition $\hat{\psi} = \hat{\psi}_c$ at $l = l_c$. At $l < l_c$, kinking of the interfacial crack is suppressed as K_{II} is negative for any flaws which adjoin the interfacial crack. At $l > l_c$, $K_{II} > 0$ at the tip of any flaws adjoining the interfacial crack and kinking into the adhesive layer can occur. The kinking event at $l = l_c$ is supercritical in the sense that more than sufficient energy is available to drive the kink.

The expected sequence of events in the growth of the alternating crack and the associated remote load versus crack length response for a DCB specimen is shown schematically in Fig. 14.

Consider the alternating crack such that its tip lies on the upper interface and is a finite distance $l < l_c$ from the previous kink, point (a) of Fig. 14. The interfacial crack is subjected to mixed mode loading, with a phase angle $\hat{\psi}$. Let the crack extend along the interface; $\hat{\psi}$ increases and the remote load drops in order for G_I to equal $\Gamma_I(\hat{\psi})$. When the crack reaches a point (b) on the interface $\hat{\psi}$ has increased to the critical value $\hat{\psi}_c$ and kinking out of the interface becomes possible by growth of flaws which pre-exist in the adhesive and are orientated tangentially to the interface. Kinking is a supercritical event and involves a drop in the remote load. The crack runs dynamically a short distance until it reaches a point (c) in Fig. 14. The presence of tensile residual stress in the adhesive layer causes the crack to grow under decreasing remote load along a curved trajectory and it grows through points (c) and (d) towards the opposite interface. When the crack tip is close to the opposing interface at point (e) it is repelled by the stiffer substrate (aluminium is much stiffer than epoxy), and the crack tip adopts a reversal in curvature (see Fig. 6f); the remote load is increased in order for the crack to continue to propagate. The crack grows almost tangentially to the interface, and becomes an interfacial crack on the lower interface, point (f) of Fig. 14. Continued propagation is interfacial, and the cycle of events is repeated.

4.7. *Wavelength of alternating crack trajectory*

Akisanya and Fleck [1] have predicted the dependence of l_c/h upon α, β, $K_{II}^{\infty}/K_I^{\infty}$, s/h and $\zeta = \sigma_0\sqrt{h}/\sqrt{\bar{E}_*\Gamma_I(\psi_c)}$, where $\bar{E}_*$ is defined by,

$$\frac{1}{\bar{E}_*} = \frac{1}{2}\left[\frac{1}{\bar{E}_1} + \frac{1}{\bar{E}_2}\right]\frac{1}{\cosh^2(\pi\varepsilon)} \tag{9}$$

and $\bar{E} = E/(1 - \nu^2)$ is the plane strain Young's modulus. For $K_{II}^{\infty} = 0$, and for given values of α, β, and s/h, the relative half wavelength l_c/h increases with increasing ζ, see Fig. 15.

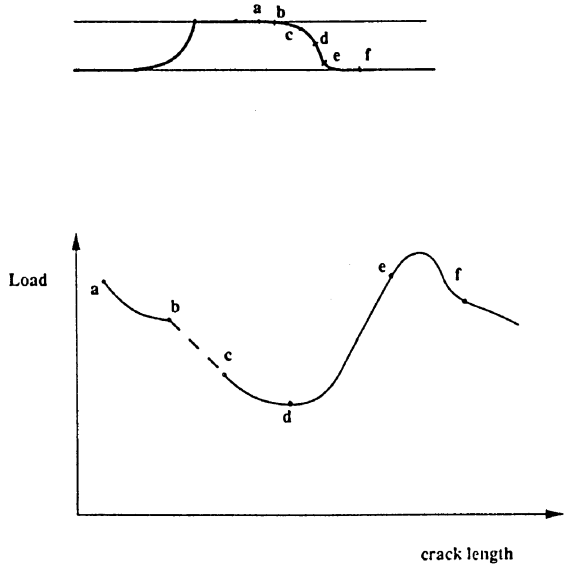

Fig. 14. Sequence of events in the growth of the alternating crack and the associated remote load versus crack length response.

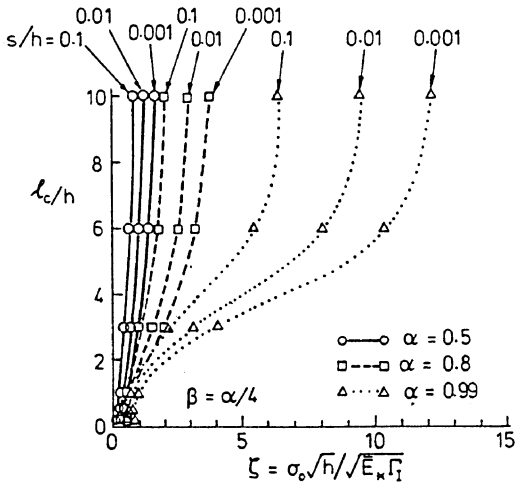

Fig. 15. The dependence of the relative half wavelength of the alternating crack l_c/h on the parameter $\zeta = \sigma_0\sqrt{h}/\sqrt{\bar{E}_*\Gamma_I}$. Taken from Akisanya and Fleck [1].

The predicted values of l_c are compared with the measured values in Fig. 16, for the case of symmetrical DCB specimens. The variation in the measured values of l_c is due to variation of h and σ_0. We note that best agreement between theory and experiment is achieved by assuming a flaw length of $s = 10\,\mu m$ on the interface. Observed values of flaw size were of this order of magnitude. The predicted magnitude of l_c is not sensitive to the assumed value of s when $\zeta \ll 1$.

The effect of residual stress level σ_0 and layer thickness h upon the half wavelength l_c of the wavy crack is shown in Fig. 17. We note that l_c increases with increasing σ_0 and increasing h. The predicted trends are in good agreement with the observations, when we assume $s = 10\,\mu m$.

The macrosopic toughness of the alternating crack is typically twice that of the interfacial crack, for remote mode I loading ($\phi = 0°$), see Fig. 10. Chai [22] observed a similar increase in macroscopic toughness for the alternating crack path, in a similar aluminium/epoxy system. Simple energy arguments would suggest that the macroscopic toughness decreases with an increase in stored elastic strain energy in the layer. We note from Fig. 11 that the macroscopic toughness of the alternating crack path *increases* with $\xi = \sigma_0\sqrt{h}/\sqrt{\bar{E}_2\Gamma_I(\hat{\psi})}$. This is not surprising when we consider that the macroscopic toughness is an average measure of the toughness associated with the alternating crack path. The cracking pattern involves interfacial crack growth with a varying phase angle $\hat{\psi}$, crack kinking and crack advance across the adhesive layer. An increase in the residual tensile stress in the layer decreases the phase angle $\hat{\psi}$ on the interfacial crack prior to kinking and increases the interfacial toughness contribution to the average macroscopic toughness.

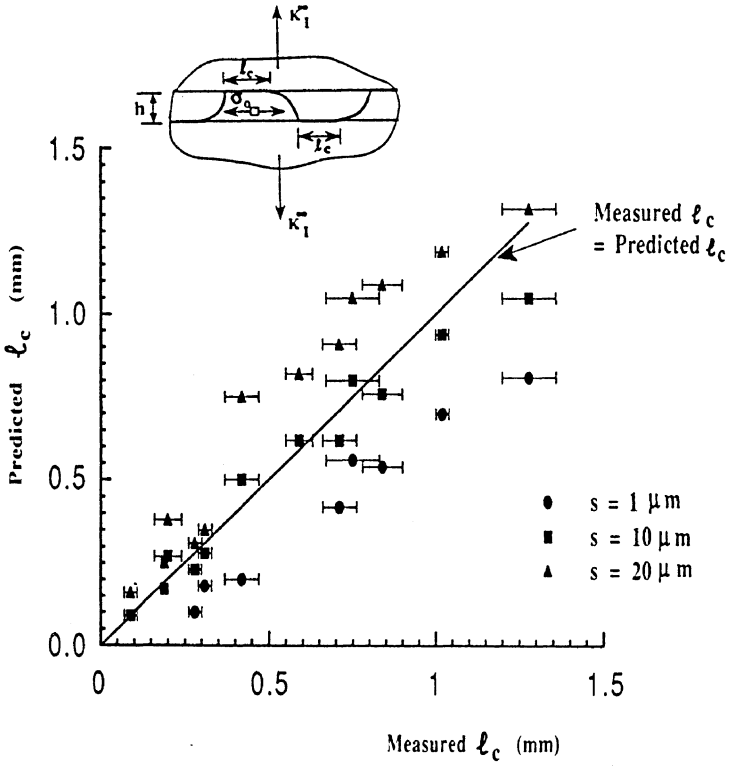

Fig. 16. The predicted versus measured values of the critical length l_c when the alternating crack leaves the interface for different values of assumed flaw size s. The error bars represent the standard deviation of the measured values of l_c for the symmetric DCB specimens.

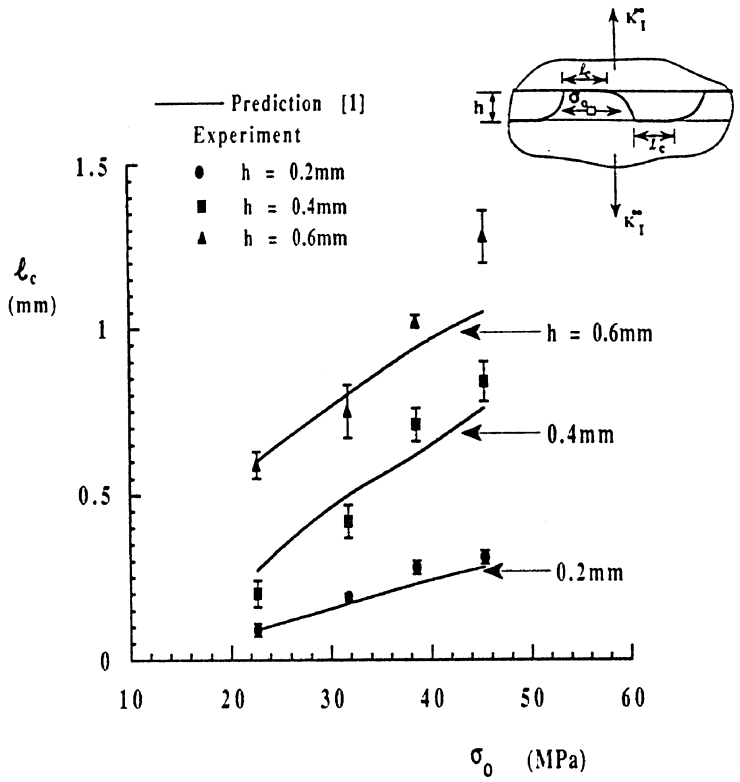

Fig. 17. Effect of the residual stress σ_0 and the layer thickness h upon the half wavelength l_c of the alternating crack for the DCB specimens under a remote mode I loading. The predicted values are for a flaw size $s = 10\,\mu m$.

The alternating crack morphology was also observed in the asymmetric DCB beam specimens for $-0.2 < K_{II}^\infty/K_I^\infty < 0.35$. This range of mode mix is in rough agreement with the predicted range $|K_{II}^\infty|/K_I^\infty < 0.38$, [1]. When $K_{II}^\infty/K_I^\infty > 0$, the length of interfacial crack growth along the upper interface l_1 is less than the growth increment along the lower interface l_2 prior to kinking. Figure 18 shows the effect of remote shear on l_1 and l_2, for specimens with $\sigma_0 = 31.8$ MPa, and $h = 0.4$ mm. With increasing K_{II}^∞/K_I^∞, the length l_1 decreases whilst the length l_2 increases, as expected. The predicted values of l_1 and l_2 from the analysis of Akisanya and Fleck [1] are in reasonable agreement with the observed response.

5. Concluding discussion

The fracture resistance of the interface between aluminium and epoxy has been characterised over a range of mode-mix using Brazil nut and asymmetric DCB specimens. The fracture resistance increases with the increase in mode mix. The crack path is dependent upon the sign and magnitude of the loading phase $\hat{\psi}$ at the crack tip. Crack propagation is along the lower interface when $\hat{\psi}$ is positive and along the upper interface when it is negative.

The experiments illustrate the effects of the residual stress σ_0 in the adhesive layer and the layer thickness h upon the wavelength of a crack that grows by alternating between the two interfaces. The wavelength increases with increasing σ_0 and h.

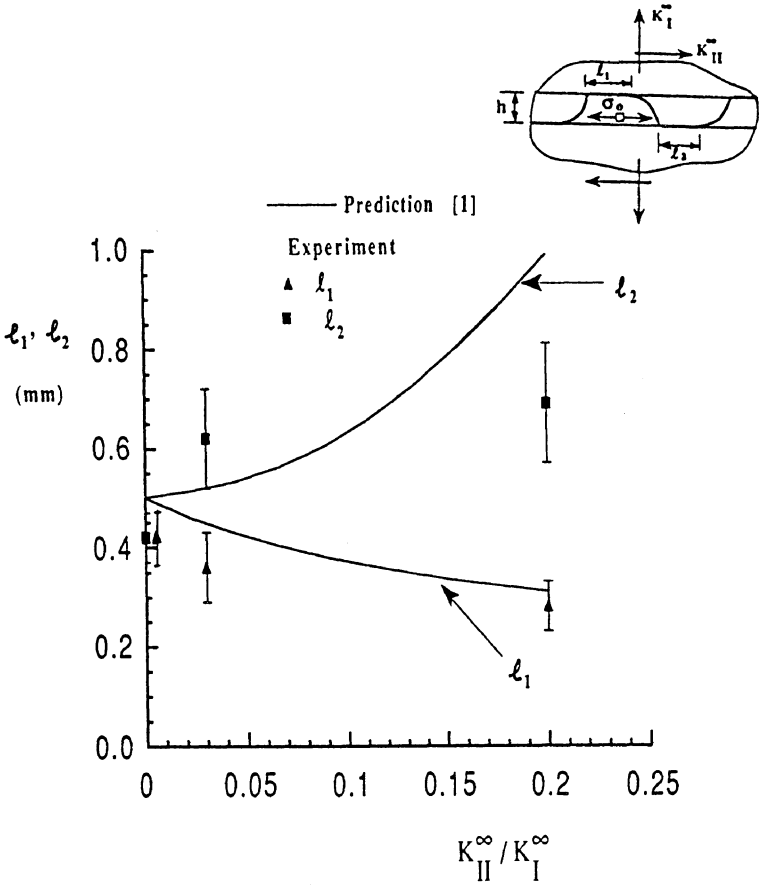

Fig. 18. Effect of remote shear upon the critical lengths l_1 and l_2 of the alternating crack for the asymmetric DCB specimens. $\sigma_0 = 31.8$ MPa, $h = 0.4$ mm, and $s = 10$ μm.

The probability of each failure mechanism is shown in Fig. 7, for $\sigma_0 = 31.8$ MPa and $h = 0.4$ mm. As the layer thickness h is increased, there is a slight increase in the proportion of fracture surface created by a serrated interfacial crack, and by in-layer cracking, and a slight decrease in the occurrence of unserrated interfacial cracking and the alternating crack morphology. When the residual stress level is increased the serrated interfacial and alternating crack paths become more common, while the unserrated interfacial and in-layer cracking patterns become less common.

We conclude that the local cracking pattern in an adhesive joint strongly affects the measured toughness. For a crack that grows by alternating between the interfaces, the average toughness is more than twice the interfacial toughness. When the crack grows interfacially and interacts with flaws in the adhesive to form a serrated crack path, the macroscopic average toughness is approximately twice the interfacial toughness.

Appendix A. Calibration of specimen geometries.

Asymmetric double cantilever beam specimens

The DCB specimen geometry consists of two strips of the same material with height h_1 and h_2, joined by a thin layer of adhesive, as shown in Fig. 4a. A crack of length L exists

between the two arms of the specimen. The upper and lower arms of the specimen are subjected to a load P per unit thickness. The K calibration for the homogeneous geometry neglecting the presence of the adhesive layer and for infinitely long strips has been given by Bao et al. [16].

The total strain energy release rate for coplanar crack advance is,

$$G = \frac{6(PL)^2}{\bar{E}_1 h_2^3}(1 + \lambda^3)\left[1 + 0.677\mathrm{B}(\lambda)\frac{h_2}{L}\right]^2, \tag{A.1}$$

where $\lambda = h_2/h_1$, $\bar{E}_1$ is the plane strain Young's modulus of the strips and,

$$B(\lambda) = 1.120 - 0.695(\lambda - 0.585)^2. \tag{A.2}$$

In a homogeneous asymmetric DCB specimen, with $\lambda < 1$, the phase angle $\phi = \arctan(K_{\mathrm{II}}^{\infty}/K_{\mathrm{I}}^{\infty})$ of crack tip loading is given by,

$$\phi = -\arctan\left[\left(\frac{1 + 0.677\mathrm{B}(\lambda)\dfrac{h_2}{L}}{1 + 0.677\mathrm{B_I}(\lambda)\dfrac{h_2}{L}}\right)^2 \frac{1}{\sin^2\Phi} - 1\right]^{\frac{1}{2}}, \tag{A.3}$$

where

$$\Phi(\lambda) = \tfrac{1}{2}\pi(0.574 + 0.033\lambda + 0.805\lambda^2 - 0.413\lambda^3), \tag{A.4}$$

$$B_I(\lambda) = 1 + 0.546(1 - \lambda). \tag{A.5}$$

Equation (A.3) shows that for a given value of L/h_2, ϕ decreases as h_1/h_2 increases. For the symmetric DCB specimen $h_1 = h_2$ and $\phi = 0$.

Brazil nut specimen

Consider a Brazil nut specimen of radius R, with a center crack of length $2L$, as shown in Fig. 4b. The specimen is subjected to a diametral compressive load P per unit thickness of the disk. The loading phase is controlled by the compression angle θ, as shown in Fig. 4b. For a homogeneous disk, the specimen is in pure mode I ($\phi = 0°$) when $\theta = 0°$, and is in pure mode II ($\phi = 90°$) when $\theta = 25°$. A detailed analysis of the Brazil nut specimen is given by Atkinson et al. [17].

The stress intensity factors at the crack tip for the homogeneous specimen are,

$$K_{\mathrm{I}}^{\infty} = Q_1 PR^{-1/2}, \quad K_{\mathrm{II}}^{\infty} = \pm Q_2 PR^{-1/2}, \tag{A.6}$$

where the plus sign is for tip A and the minus sign is for tip B of Fig. 4b. The non-dimensional factors Q_1 and Q_2 are functions of the relative crack length L/R and θ, and are given in polynomial form by Atkinson [17].

Acknowledgements

The authors are grateful for helpful discussions with Prof. J.W. Hutchinson. They wish to thank Ciga-Geigy Ltd., Duxford, England for provision of the epoxy. A.R.A. is grateful for financial support from Cambridge Commonwealth Trust.

References

1. A.R. Akisanya and N.A. Fleck, *International Journal of Fracture* 55 (1992) 29–45.
2. W.A. Zdaneiwski, J.C. Conway and H.P, Kirchner, *Journal of American Ceramic Society* 70 (1987) 104–118.
3. H.C. Cao, M.D. Thouless and A.G. Evans, *Acta Metallurgica* 36 (1988) 2037–2046.
4. B.J. Dalgleish, M.C. Lu and A.G. Evans, *Acta Metallurgica* 38 (1988) 2029–2035.
5. H. Tada, P.C. Paris and G.R. Irwin, *Stress Analysis of Cracks Handbook*, Del Research, St. Louis, MO (1985).
6. H.C. Cao and A.G. Evans, *Mechanics of Materials* 7 (1989) 295–304.
7. J.S. Wang and Z. Suo, *Acta Metallurgica* 7 (1990) 1279–1290.
8. M.D. Thouless, *Acta Metallurgica* 36 (1990) 1135–1140.
9. J.W. Hutchinson, M.E. Mear and J.R. Rice, *Journal of Applied Mechanics* 54 (1987) 828–832.
10. N.A. Fleck, J.W. Hutchinson and Z. Suo, *International Journal of Solids and Structures* 27 (1991) 1683–1703.
11. H. Chai, *International Journal of Fracture* 32 (1986) 211–213.
12. J. Dundurs, in *Mathematical Theory of Dislocations*, American Society of Mechanical Engineering, New York (1969) 70–115.
13. J.R. Rice, *Journal of Applied Mechanics* 55 (1988) 98–103.
14. Z. Suo and J.W. Hutchinson, *Materials Science and Engineering* A107 (1989) 135–143.
15. M.Y. He and J.W. Hutchinson, *Journal of Applied Mechanics* 56 (1989) 270–278.
16. G. Bao, S. Ho, B. Fan and Z. Suo, *International Journal of Solids and Structures* (1990) submitted.
17. C. Atkinson, R.E. Smelser and J. Sanchez, *International Journal of Fracture* 18 (1982) 279–291.
18. B.M. Liaw and M. Kamel, *International Journal of Engineering Science* 28 (1990) 1053–1065.
19. K.M. Liechti and Y.S. Chai, *Journal of Applied Mechanics* 28 (1992) 295–304.
20. A.G. Evans and J.W. Hutchinson, *Acta Metallurgica* 37 (1989) 909–916.
21. J.W. Hutchinson and Z. Suo, *Advances in Applied Mechanics* 29 (1992) 63–191.
22. H. Chai, *Engineering Fracture Mechanics* 24 (1986) 413–431.